Effects of preparation on catalytic, magnetic and hybrid micromotors on their functional features and application in gastric cancer biomarker detection

Daniela F. Báez[a,b,c,*], Gabriel Ramos[d], Alejandro Corvalán[c,e], María Luisa Cordero[d], Soledad Bollo[a,b,c], Marcelo J. Kogan[b,c,*]

[a] Centro de Investigación de Procesos Redox (CiPRex), Facultad de Ciencias Químicas y Farmacéuticas, Universidad de Chile, Santiago, Chile
[b] Departamento de Química Farmacológica y Toxicológica, Facultad de Ciencias Químicas y Farmacéuticas, Universidad de Chile, Santiago, Chile
[c] Advanced Center for Chronic Diseases (ACCDiS), Facultad de Ciencias Químicas y Farmacéuticas, Universidad de Chile, Santiago, Chile
[d] Departamento de Física, Facultad de Ciencias Físicas y Matemáticas, Universidad de Chile, Avenida Blanco Encalada 2008, Santiago, Chile
[e] Departamento de Hematología y Oncología, Facultad de Medicina, Pontificia Universidad Católica de Chile, Av Libertador Bernardo O'Higgins 340, Santiago, Chile

ARTICLE INFO

ABSTRACT

Artificial micromotors evolve to improve multitasking performance in different research areas, and different power sources are combined to give rise to hybrid micromotors. Such combinations can alter physical features and influence movement aspects that until now have not been taken into account. Here, we comparatively studied how physical features of magnetic (erGO/Ni), catalytic (erGO/Pt), or dual propulsion (erGO/Pt-Ni and its inverted form erGO/Ni-Pt) micromotors can influence direction and speed. The results showed that erGO/Pt and erGO/Ni microtubes presented different growth modes dependent on experimental conditions. For the hybrid form, similar features were observed but thicker and shorter than their individual versions. The catalytic motion comparison demonstrated that the main movement pattern was circular, and erGO/Pt micromotors were faster than the hybrid form, reaching speeds up to 360 μm s^{-1}. The addition of a third material decreased significantly the speed especially when nickel was in the last layer, demonstrating that the order in which metallic elements are deposited is relevant and influences the speed. The erGO/Pt microtubes were selected to detect Reprimo, a gastric cancer biomarker. The detection assay (static or catalytic conditions) relies on the *turn-off/turn-on* fluorescence recovery due to the hybridization process between the Reprimo probe tagged with a fluorescein amidine dye and target biomarker Reprimo ssDNA, followed by its detachment from microtube. The catalytic detection results have shown to possess great selectivity as well as good reproducibility and can become a promising strategy for qualitative or quantitative detection of Reprimo or other circulant cancer biomarkers based on DNA.

1. Introduction

The design and development of artificial micromotors continue receiving significant attention in the last decade since these microdevices have the fantastic ability to perform different complex tasks while they are in continuous motion [1–3]. The motion of these microengines is sometimes produced by a catalytic reaction or by converting an external source of energy, e.g., magnetic, electrical, or thermal, into mechanical work [4,5]. This ability has enabled its use in multiple areas as environmental remediation [6,7], cargo delivery [8–10], and biosensing applications [11,12]. The last one includes the detection of

nucleic acids, protein, cancer cells, among others, in which the use of micromotor has demonstrated potentiality as a sensing device in motion-based studies. However, to date, there are only a few reports of micromotors for applications in the detection of DNA biomarkers associated with cancer but not in gastric cancer [13,14]. Gastric cancer (GC) could be a curable disease if it is diagnosed at the early stages. However, at this phase gastric cancer is asymptomatic, and therefore, most cases are diagnosed once the condition is at advanced stages. Among the methodologies developed to detect cancer biomarkers are polymerase chain reaction (PCR) [15], electrophoresis [16], enzyme-linked immunoadsorption assay (ELISA) [17] and surface plasmon

spectroscopy [18], among others. However, despite the high sensitivity of these techniques, they require a high sample volume and preparation time, delaying the analysis and therefore the result. In this sense, the use of micromotors could be useful as part of detection systems because they can be in constant movement within the sample, increasing the chances of interaction with target molecules (biomarker) and decreasing the detection and analysis time.

The current micromotor morphologies most reported for sensing applications are spherical [5], helical [19,20], and tubular forms, all of which are closely related to their methods of preparation. The e-beam evaporation and glancing angled deposition techniques have been generally used to synthesize the spherical and helical forms, while roll-up technology and the template-assisted electrochemical method have been used to develop the tubular shape [1,21–23]. The last method stands out from the rest since it starts from a simple and inexpensive redox reaction and can obtain a large quantity of material compared to the roll-up technology. Additionally, new kinds of microtubular motors can be obtained with this method, by either changing the composition or the geometric template dimensions.

One of the most popular propulsion mechanisms of microtubular motors is produced by a chemical reaction that occurs inside the tube; this produces bubbles that are self-expelled from one output of the tube and creates a propulsion force that is contrary to the bubble direction [1,24,25]. The most common catalysts used are MnO_2, Pd, Ir, and Pt, which decompose hydrogen peroxide (H_2O_2), used as fuel, into O_2 bubbles and water, and noncatalysts, such as Mg or Zn, that react in acidic environments to produce hydrogen bubbles [26]. Microtubular motors with inner platinum can achieve higher speed in the presence of a minimum concentration of H_2O_2 and move for a long time compared with other catalytic micromotors, so they are still widely developed despite the constant search for new biocompatible sources of fuel [1,27]. However, due to their small size, these self-propelled micromotors are highly influenced by Brownian behavior, which means that the displacement occurs in random directions regardless of their composition [28]. Moreover, it is not possible to stop them, and therefore, movement control and guidance represent a great challenge. To address this limitation, efforts have been made to design and incorporate more than one power source that accomplishes these requirements, forming a hybrid microengine. Materials such as polymers, metal oxides, carbon nanomaterials (graphene derivates and carbon nanotubes), and magnetic compounds (iron, cobalt, nickel) have been used to modify propulsion aspects including direction control and speed or the micromotor's functionality by modifying its surface to perform different tasks at the same time.

With regard to magnetic and catalytic hybrid microtubular motors, which offer a double function since they can be guided while they are self-propelled, only a few reports are found. For instance, Singh et al., developed a zirconia-graphene/platinum microtubular motor to capture nerve agents; they added an extra nickel layer to isolate and recover them magnetically [29]. Vilela et al., designed a multilayer micromotor based on graphene oxide (GO) and a nickel-platinum (Ni-Pt) inner layer for heavy metal remotion from water [7]. Additionally, Molinero-Fernandez et al., developed a similar microtubular motor for mycotoxin analysis [30], and recently, Liang et al., described the development of titanium microtubular motor coated with silica and with platinum and magnetic nanoparticles inside for collection and degradation of pollutants [6]. All the examples mentioned above focused mainly on environmental applications of the hybrid microtubular motors, arbitrarily leaving the magnetic component in between the metallic deposits and only for collection purposes. Instead, the platinum deposit is exposed to the inside of the microtube and used for self-propelling motion.

Nevertheless, the influence of the order in which the metals have been deposited on the final type and speed of movement has not been studied to date. The geometrical characteristics of the resulting hybrid microtubular motors have not been taken into account on motion aspects and have not been compared with their individual versions, such as the reduced graphene oxide and platinum (rGO/Pt) or nickel (rGO/Ni) micromotors with the rGO/Ni-Pt and inverted rGO/Pt-Ni micromotors.

In this work, four microtubular motors consisting of electrochemically reduced graphene oxide (erGO), nickel, and platinum were prepared: the erGO/Pt and erGO/Ni micromotors, which present magnetic or self-propelled motion, respectively, and two hybrid types, erGO/Ni-Pt with its inverted form erGO/Pt-Ni. For these last two, both magnetic and self-propelling motion are expected. We comparatively studied how the geometrical features, the number of metallic deposits, and the deposition order influence the motion aspects, including direction control and speed. Moreover, to our understanding, neither erGO/Ni nor erGO/Pt-Ni microtubular motors have been described to date.

A functional assay is also presented by using micromotors as a sensing system to detect the methylated promoter region of Reprimo (RPRM). RPRM is a short, 303 bp, coding gene, regulated by DNA methylation of its promoter region. Methylation leads to a functional silencing of RPRM which is associated with the loss of tumor suppressor properties and associated with the development of gastric cancer. Methylation of the promoter region of RPRM has been proposed as a potential biomarker for non-invasive detection of gastric cancer since its DNA can be extracted from serum and plasma samples in cancer patients but is rarely found in healthy controls [31–34]. The detection procedure detailed in the following sections relies on the well-known quenching effect that reduced GO produces to some fluorescent molecules adsorbed on its surface [35]. In this case, the complementary Reprimo ss-DNA probe, tagged with a fluorescein amidine dye (RPRM/FAM) was adsorbed on erGO, the outer layer of the microtubes. The quenched fluorescence was used as a strategy to make a *turn-off/turn-on* detection system based on the hybridization process between both ssDNA (RPRM/FAM probe and target RPRM), which leads to a recovery of the fluorescence signal due to the formation of the double-stranded DNA and its detachment from the rGO microtube. Besides, the detection of this GC biomarker is reported in static and catalytic conditions. The last one assessed by the addition of hydrogen peroxide used as fuel, to investigate the effect of catalytic motion on the detection. To the best of our knowledge, this is the first time that micromotors are applied in the detection of DNA biomarkers associated with gastric cancer.

2. Experimental section

2.1. Materials and reagents

Cyclopore polycarbonate membranes with 5 μm tubular-shaped pore diameters were purchased from Whatman, USA (catalog No 7060-2513). Methylene chloride, isopropanol, and ethanol were obtained from Sigma Aldrich. Hydrogen peroxide (H_2O_2, 32 wt%), platinum plating solution, nickel chloride, nickel (II) sulfamate tetrahydrate, boric acid, and sodium cholate (SCh) were purchased from Merck, and alumina slurry was purchased from G. Busch & Cia. Ltda. Our lab previously synthesized and characterized graphene oxide through a modified Hummer's method [36], and this reagent was dry-stored. Ultrapure water was obtained from a Millipore water purification system ($\geq$ 18 MΩ, Milli-Q, Millipore) and used to prepare all solutions.

All the synthetic DNA oligonucleotides were purchased from Integrated DNA Technologies (IDT, Coralville, IA, USA) and the sequences are enumerated below:

- Reprimo ssDNA probe (RPRM/FAM): FAM- 5′AAAAACGAACGAA CGCCGCGAACGACGCGAATCCGA-3′
- Target Reprimo ssDNA (RPRM): 5′-TCGGATTCGCGTCGTTCGCG GCGTTCGTTCGTTTTT-3′
- Non complementary ssDNA (NC): 5′-CTCAGCAAGCCTCAATG-3′

2.2. Solutions

0.10 mg of graphene oxide was dispersed in a solution consisting of H_2SO_4 (0.1 M) and Na_2SO_4 (0.1 M) [27]. The nickel solution was prepared according to reference [37]. Sodium cholate was prepared by dissolving 0.02 g in 1 mL of Milli-Q water.

All ssDNA oligonucleotides were reconstituted in TE buffer solution (0.20 M Tris−HCl, 20 mM EDTA, pH 7.5), aliquoted in 100 µM stock solution, and kept frozen until use. The DNA immobilization was made using TE buffer saline solution (containing NaCl 100 mM, pH 7.5).

2.3. Preparation of micromotors

Template electrochemical deposition of the microtubes was conducted by a CHI 760 potentiostat (CH Instrument, Inc., Austin, Tx, USA); a Pt wire and an Ag/AgCl (3 M KCl) electrode were used as auxiliary and reference electrodes, respectively. A polycarbonate membrane was sputtered on one side with a gold film (70 nm) and used after as a template and working electrode. The sputter was performed using a Cressington Sputter Coater 108 auto with MTM-20 thickness controller equipment under vacuum at room temperature and 40 mA.

First, the membrane was assembled into a customized Teflon cell where 10 mL of graphene oxide (GO) solution was added to the cell and electrochemically reduced over the wall pores of the membrane (Fig. 1, step a) at room temperature using cyclic voltammetry (CV, over +0.30 to –1.50 V, at 50 mV s^{-1}, for five cycles). Subsequently, a layer of platinum, nickel or both was electrodeposited over the surface of erGO (Fig. 1, step b). The platinum layer was galvanostatically deposited at -2.0 or -20.0 mA for 300, 500, 1000 and 2000s. Nickel was deposited amperometrically at -1.30 V for 1.0 C and 4.0 C. To release the microtubes from the template membrane (Fig. 1, step c), the gold layer was completely removed by mechanical hand polishing with a 5.0 µm alumina slurry, and then the membrane was dissolved in methylene chloride for 15 min. Then, the microtubes were collected by centrifugation at 3835 g for 3 min. Afterward, successive washes with isopropanol followed by ethanol and ultrapure water (three times) were performed with a 3 min centrifugation at 3835 × g between each wash. All microtubes were stored in ultrapure water at room temperature when not in use. The template preparation method resulted in reproducible micromotors.

2.4. Immobilization of ssDNA RPRM/FAM probe on micromotors

To immobilize the RPRM/FAM probe (λ_{ex}: 495 nm, λ_{em}: 520 nm) onto the erGO micromotor surface, 200 µL of RPRM/FAM probe (10 µM), prepared in TE buffer saline solution, was added dropwise to the microtubes. The mixture solution was incubated overnight with gentle magnetic stirring at room temperature. Then, the modified RPRM/FAM/erGO/Pt micromotors travel decanted for 50 min, the supernatant was extracted and 200 µL of TE buffer solution was added (repeated two-times), then the RPRM/FAM/erGO/Pt micromotors were stored in TE buffer solution at 4.0 °C.

2.5. Fluorescence recovery assay

A volume of 10 µL of the modified RPRM/FAM/erGO/Pt micromotors solution and 2.0 µL of sodium cholate (2.0 % wt final) was added into a 0.5 mL tube maintained without movement. Then, 2.0 µL of different solutions and concentrations were added depending on the study. For catalytic detection, H_2O_2 was added (1.5 % wt final) and for the detection in static conditions, TE buffer solution was added in replacement of the fuel. The fluorescence intensity recovery was monitored at different times by taken 0.5 µL of the mixture, placed onto a clean glass slide and measuring the fluorescence intensity of the droplet.

2.6. Instruments

A scanning electron microscope (SEM; Jeol JSM IT300 LV) coupled with an energy-dispersive spectrometer (EDS; Oxford Instruments, U.K.) was used to assess the morphology and elemental mapping of the micromotors.

To perform and record the movement, 2.0 µL of freshly prepared 2.0 wt% sodium cholate (Sch) was placed onto a clean glass slide, and then 2.0 µL of each type of micromotor (erGO/Pt, erGO/Pt-Ni or erGO/Ni-Pt) was added. Finally, 2.0 µL of H_2O_2 solution at different concentrations (wt%) was added to induce the self-propelled movement. For magnetic motion, a magnet was drawn close to the left side of the glass slide. For magnetic motion, a magnet was drawn close to the left side. Magnetic field intensity was measured using a gaussmeter (PCE-MFM 3000, PCE Instruments).

To investigate the microtube motion, movie clips were recorded during a given time using an inverted microscope Nikon TS-100 equipped with a 10X or 40X objective and an Andor Zyla digital camera. The tracking and analysis of the video clips were conducted using MATLAB software.

Fluorescence images were recorded using an inverted Olympus CKX41 microscope with filter and Nikon camera DS-Fi 2. The quenching effect and the recovered fluorescence intensity produced by the hybridization process was estimated by analyzing the corresponding images using the ImageJ software.

3. Results

The micromotors were prepared through the template-assisted electrochemical method following the protocol described by Wang's group [11] with some modifications; the step sequence is illustrated in Fig. 1. First, an outer layer of electrochemically reduced graphene oxide (erGO) was deposited onto the pore wall of a microtubular membrane (step a) to give support to a second metallic layer. In step b, a single metallic layer of platinum (Pt) or nickel (Ni) was deposited onto the erGO surface to form the erGO/Pt and erGO/Ni microtubes, respectively. Subsequently, a third layer can also be formed by a second metal deposition, Pt or Ni, to form the erGO/Pt-Ni and the erGO/Ni-Pt hybrid micromotors. It should be noted that erGO/Ni and erGO/Pt-Ni micromotors have not been reported to date. Finally, the four kinds of microtubes were removed from the membrane (step c) by dissolution and
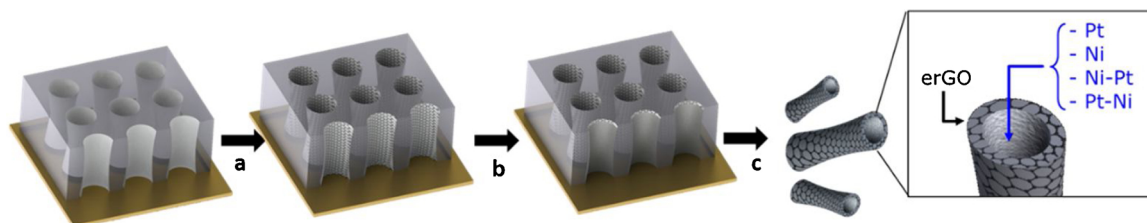

Fig. 1. Schematic illustration of the template-assisted electrochemical deposition method to prepare the microtubular motors, where (a) represents the erGO deposition; (b), metallic deposition; and (c), the release of the microtubes from the membrane.

stored in Milli-Q water. The motion of the microtubular motors is performed through the addition of hydrogen peroxide (H_2O_2) in different concentrations, by an approaching magnet or both at the same time.

The graphene oxide (GO) characterization and the electrochemical profile for the deposition of reduced graphene oxide (erGO) are shown in Supplementary Figure S1(a–c). Figure S1a depicts a characteristic Raman spectrum for GO showing the G (~ 1580 cm^{-1}) and D peak (~ 1350 cm^{-1}). From the intensities of these two bands, the ID/IG ratio was calculated as a measure of the defect degree related to in-plane vacancies or impurities as interstitial or edge heteroatoms coming from the functional groups present in the carbon nanomaterial. Figure S1b shows the contribution of those carbon functional groups. The contribution located at 284.6 eV can be associated with the C−/C=C groups, whereas those observed at 286.8 eV, 288.2 eV, and 289.2 eV correspond to the C−O, C=O, and O−C=O groups, respectively. Figure S1c, shows a clear reduction peak is observed at -0.870 V (vs. Ag/AgCl) and attributed to the reduction of functional groups present in GO (ketones, hydroxyls, aldehydes, and carboxylic acids, among others) [5]. The current intensity of the reduction signal decreases with the scan number, indicating that most of the oxygen moieties have been successfully reduced. Fig. 2A shows the potential *vs.* time profile obtained for the galvanostatic electrodeposition of platinum onto the erGO surface to form the erGO/Pt microtubes. The curves obtained are similar to those registered by other researchers for the deposition of platinum nanoparticles via an open circuit potential method over a microelectrode surface [38,39]. When the current applied is – 2.00 mA during 300, 500 or 1000s, a potential of -0.250 V is reached and remains constant over time, but when the current is applied for 2000s, the potential decreases to -0.237 V, and then remains constant over time. Fig. 2A (a–d) shows one representative SEM image of the obtained erGO/Pt microtubes synthesized under these experimental conditions. The continuous growth of the microtubes with longer deposition times was observed. Measured average lengths of 4.15 ± 0.68, 6.20 ± 0.10, 6.96 ± 0.49 and 12.3 ± 0.60 μm were obtained for 300, 500, 1000 and 2000s, respectively (at least ten microtubes were measured). The same behavior was recently reported by Pumera et al., who synthesized platinum micromotors using a 3 μm pore diameter membrane [40,41].

All microtubes obtained from these experimental conditions were subjected to a rapid test of motion and showed no self-propulsion
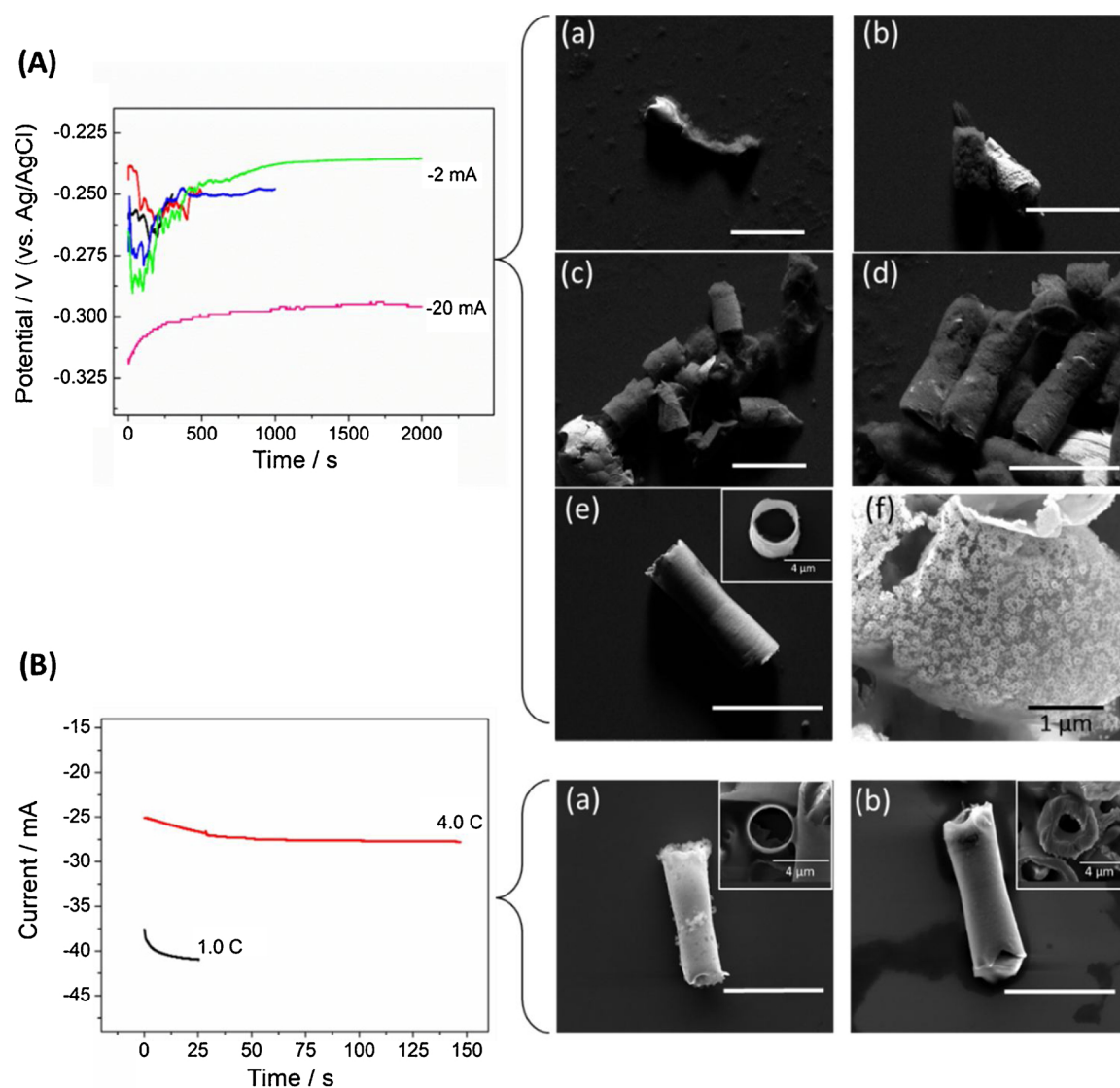

Fig. 2. (A) Potential *vs.* time profile for the platinum (Pt) deposition and SEM images obtained for the erGO/Pt microtubes at -2 mA for 300 s (black line, image a); 500 s (red line, image b); 1000s (blue line, image c) and 2000s (green line, image d). At -20 mA for 2000s (pink line, images e–f). (B) Current vs. time profile for nickel (Ni) deposition and SEM images for the erGO/Ni microtubes obtained at a charge of 1 C (black line, image a) and 4 C (red line, image b). Inset images correspond to the top view of the microtube; scale bar is 10 μm unless otherwise specified.(For interpretation of the references to colour in the Figure, the reader is referred to the web version of this article).
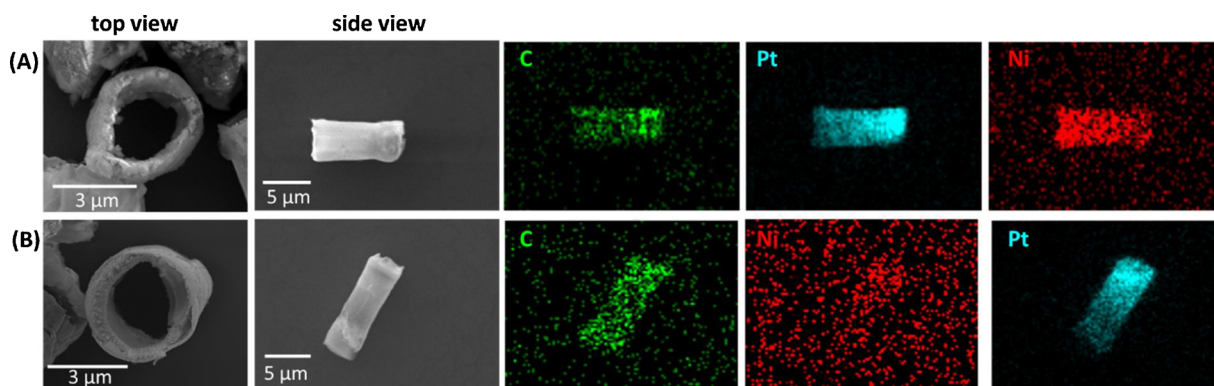
Fig. 3. Top and side view of SEM images and EDX mapping analysis of carbon (green), platinum (cyan) and nickel (red) for (A) microtubes of erGO/Pt-Ni and (B) microtubes of erGO/Ni-Pt. (For interpretation of the references to colour in the Figure, the reader is referred to the web version of this article).

response even at high concentrations of hydrogen peroxide. This behavior might be due to the inhibition of the bubble formation, growth and ejection since the process is dependent on the geometric symmetry and the length of the microtube where fluctuations inside the tubular structure may eventually inhibit this process changing the rate of bubble formation and disturbing the motion [42]. For this reason, we decided to increase the applied current from -2.0 mA to -20.0 mA for 2000s. In Fig. 2A (pink curve), a negative shift in potential to -0.300 V can be seen, in comparison to those obtained at -2.0 mA. Fig. 2A (e) depicts that the microtubes prepared under this experimental condition presented an entire tube-shaped morphology, a homogeneous surface with geometric dimensions of 12.6 ± 0.36 μm length, a 4.15 ± 0.26 diameter and a 0.22 ± 0.03 μm thickness. Fig. 2A (f) shows the platinum nanoparticles viewed inside of the microtube with an average diameter size of 82.70 ± 2.70 nm, confirming its deposition. These results indicate that the electrodeposition time of platinum and the current intensity applied are crucial for the formation and stability of the erGO/Pt microtube structure. A rapid test of motion showed clear self-propulsion movement of the microtubes (Supplementary Video 1) and is the reason why we selected this experimental condition for erGO/Pt microtube preparation. The composition of erGO/Pt microtubes was analyzed by energy-dispersive X-ray spectroscopy (EDX) in the mapping mode for carbon (from erGO) and platinum. The images of the elemental composition are shown in Supplementary Figure S2 (a), where it can be seen that both carbon from erGO deposition (green image) and platinum nanoparticles (cyan image) are distributed homogeneously through the microtube surface.

Fig. 2B displays the current *vs.* time plot obtained for the amperometric deposition of nickel over the erGO inner surface to form the erGO/Ni microtubes. Two charges were studied in this case to verify differences in physical features and magnetic motion. A fixed potential of -1.300 V (vs. Ag/AgCl) was applied for the necessary time to reach a charge value of 1.0 C and 4.0 C, the black and red lines, respectively. The charge, obtained from the area under the curve, can be easily obtained from this electrochemical response. It can be observed that in both cases when the potential is applied, the current has an initial increase attributed to the formation of nickel species inside the erGo surface. Under these experimental conditions, erGO can still be reduced [43,44]. From SEM images of the erGO/Ni microtubes presented in Fig. 2B (a–b), it can be seen that the microtube formation process was different from that obtained for erGO/Pt. Both conditions studied were sufficient to form and maintain the structure of the microtube with similar geometric dimensions of 11.9 ± 0.5 μm length and 4.01 ± 0.03 μm diameter (at least ten microtubes were measured for both types). However, the insets of Fig. 2B (a–b) showed a dramatic difference in the microtube thickness, changing from 0.145 ± 0.01 μm when the deposited charge was 1.0 C to 1.24 ± 0.10 μm when the charge was 4.0 C, i.e., the microtubes obtained at 4.0 C are 10 times thicker. Thus, this type of micromotor presents a different mode of growth in comparison to the erGO/Pt micromotor, characterized by a constant length but a thickness that varies according to the charge selected. Both types of erGO/Ni micromotors presented unidirectional displacement toward the direction where a magnet was positioned (Supplementary Video 2). After a few seconds, it is possible to observe the formation of rows like a chain-train between the microtubes that remain even when the magnet moves away, requiring an extra power source such as agitation to disrupt this organization. The elemental composition of the erGO/Ni microtube under both conditions is shown in Supplementary Figure S2 (b–c) measured by EDX in mapping mode, where both carbon (green) and nickel (red) were well distributed over the microtube surface.

In efforts to obtain micromotors with better capabilities of motion and function, microtubular motors that combine both magnetic and self-propelled motion have been developed. Previously, the erGO/Ni-Pt micromotor [7,30] was developed for environmental applications, where the characterization of the dual movements has not been described. We subsequently prepared erGO/Ni-Pt and erGO/Pt-Ni microtubes, starting with the electrodeposition of erGO as previously described; then, for platinum and nickel deposition, the selected experimental conditions were -20.0 mA for 2000s and -1.30 V at a charge of 1.0 C, respectively, regardless of which metal was deposited first. The electrochemical response (not shown) was equivalent to that obtained in Fig. 2 (A and B), while the SEM images (top and side view) and the EDX mapping for the elemental composition are shown in Fig. 3A for erGO/Pt-Ni and Fig. 3B for erGO/Ni-Pt. Both microtubes presented a microtubular morphology with homogeneous topography (side view). The geometrical dimensions were similar for both with an average length and diameter of 11.70 ± 0.19 μm and 3.83 ± 0.18 for erGO/Pt-Ni and 11.50 ± 0.46 μm and 3.54 ± 0.28 μm for erGO/Ni-Pt, respectively. A thickness (top view) of 0.78 ± 0.06 μm for both micromotors was obtained. Analyzing the elemental composition for carbon (green), platinum (cyan), and nickel (red), a well-distributed deposition along the tube was observed. In summary, both types of hybrid microtubes showed similar physical features but were shorter and thicker than their individual versions.

A comparison of the self-propelled movement for erGO/Ni-Pt and erGO/Pt-Ni micromotors was evaluated and compared with that observed for erGO/Pt. The motion was performed by the addition of different concentrations of H_2O_2 as fuel and sodium cholate (SCh) 2.0 wt% (the sodium cholate has been used as surfactant to improve the bubble generation and self-propulsion in comparison of sodium dodecyl sulfate (SDS) or in the absence of surfactant (Figure S3). The erGO/Ni was excluded because it does not present a catalytic reaction with H_2O_2. In this study, we analyzed the motion of more than one hundred micromotors and found that the main movement pattern was circular with 47 % of the micromotors, followed by straight (39 %) and spiral (14 %). This tendency was observed independently of the type of micromotor
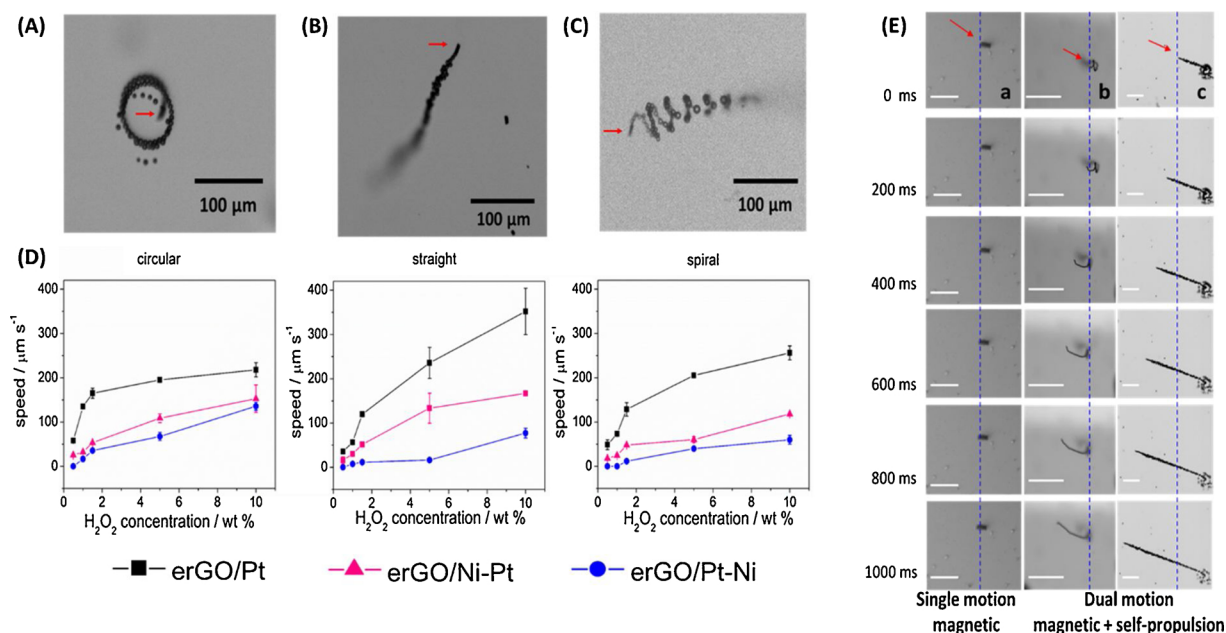
Fig. 4. Image of each pattern of movement (A) circular, (B) straight and (C) spiral, the red arrow indicates the position of the microtube. (D) Average speed for the three types of movement in different concentrations of H_2O_2 (wt%) for the erGO/Pt (black square), erGO/Ni-Pt (pink triangle), and erGO/Pt-Ni (blue circle) micromotors. The standard deviation was calculated from n = 10 trajectories. (E) Time-lapse images for (a) erGO/Ni, (b) erGO/Pt-Ni and (c) erGO/Ni-Pt micromotors depicting the movement of a magnetic guidance mode (left direction) or dual movement: self-propulsion and magnetic guidance over 1.0 s at intervals time of 200 ms (at H_2O_2 5.0 % wt). The blue dashed line indicates the initial time. The scale bar is 100 μm. (For interpretation of the references to colour in the Figure, the reader is referred to the web version of this article).

and concentration of fuel used. Fig. 4 (A, B and C) shows an image of each pattern of motion extracted from Supplementary Video 3, where the bubble wakes draw the circular (A), straight (B), and spiral (C) trajectories. In previous literature reports, different patterns of motion for nonhybrid and hybrid microtubular motors have been discussed, which could possibly be due to an asymmetric inner deposition that leads to an unbalanced formation and ejection of the oxygen bubbles but could also be due to a heterogeneous final edge tube, which twists the tube and therefore displays distinct movements [3,27,29]. In Fig. 4D, the speed *vs.* H_2O_2 (wt%) profile is separated according to the type of self-propelled movement that is displayed for the three different micromotors, erGO/Pt (black square), erGO/Ni-Pt (pink triangle), and erGO/Pt-Ni (blue circle). The average speed of the micromotors was obtained from a MATLAB-code based program that tracked the position of the micromotor in time during its trajectory. In all cases, the speed increased with increasing H_2O_2 concentration. The speed was faster for erGO/Pt micromotors for the three types of movements, reaching values up to 360 μm s^{-1} at 10 wt% of H_2O_2 in the straight movement pattern. No movement was observed for erGO/Pt-Ni at 0.5 H_2O_2 wt%, and the maximum speed reached for this type of micromotor at 10 wt% of H_2O_2 was only 137 μm s^{-1}. Instead, the erGO/Ni-Pt micromotor, which has a variable speed depending on the type of motion, reached a maximum of 170 μm s^{-1}.

In summary, the addition of a third material to form hybrid micromotors makes the microtube thicker and slower in comparison to the individual version. This reduction in the speed was more observable when the nickel was in the last layer, demonstrating that the order in which the metallic layers were deposited was not trivial and seriously influenced the speed. Since the net speed is dependent on the geometry features of the micromotors and the fluid viscosity it would be interesting to count with a theory that can determinate the speed of catalytic microtubular motors considering the thickness and elementary composition layer of the microtube and the order in which they are deposited, in that case, the equation proposed by Wang et al., could be the closest model to determinate the theoretical speed of thicker micromotors [45]. If faster hybrid micromotors are required, it is necessary to

deposit the platinum layer at the end, ensuring that it be exposed to the solution inside of the tube.

We also comparatively studied the single magnetic motion for erGO/Ni by the approaching of a magnet and the dual motion for erGO/Ni-Pt and erGO/Pt-Ni by approaching the magnet at the same time the micromotors are self-propelled (at 5.0 wt% of H_2O_2). Fig. 4E (a–c) illustrates a column of six time-lapse images extracted from Supplementary Video 4, taken every 200 ms for 1.0 s. For erGO/Ni (Fig. 4Ea), the motion started when the magnet approached enough in the left direction to apply a magnetic field intensity between ~8 m T to ~10 m T, presenting a unidirectional trajectory, with a total travel distance of 40 ± 8.0 μm. The magnet approaching effect (in the left direction) for erGO/Pt-Ni or erGO/Ni-Pt in Fig. 4E b and c, respectively. When erGO/Pt-Ni or erGO/Ni-Pt are in self-propelled mode, a breaking of the previous pattern of motion (at 5.0 wt% H_2O_2) is observed, forcing a unidirectional motion. The aggregation of micromotors, previously observed for erGO/Ni, was not observed for these kinds of hybrid micromotors. On the other hand, the magnet approach permitted an increase in the distance traveled, which was 210 ± 26.0 μm for the erGO/Pt-Ni and 593 ± 39.0 μm for the erGO/Ni-Pt micromotors. However, once the magnet is removed, the previous pattern of motion is recovered.

Thus, magnetic and self-propelled motion performed at the same time has an advantage that does not lead to aggregation, as in the erGO/Ni micromotor, and led to a single (straight) pattern of motion. However, when dual motion is required, i.e., magnetic and self-propulsion, higher concentrations of fuel (H_2O_2) are necessary to reach higher speeds than those obtained by erGO/Pt, especially when the nickel is in the last layer. This consideration should be taken into account when these kinds of hybrid micromotors are desired.

Finally, erGO/Pt microtubes were applied to the detection of the gastric cancer biomarker *RPRM*, because this type of micromotor presented higher speed at a minimum concentration of hydrogen peroxide. Fig. 5A shows a schematic illustration for the immobilization and detection procedure in static or catalytic conditions. Initially, the single-stranded RPRM/FAM probe was adsorbed over the erGO surface mostly
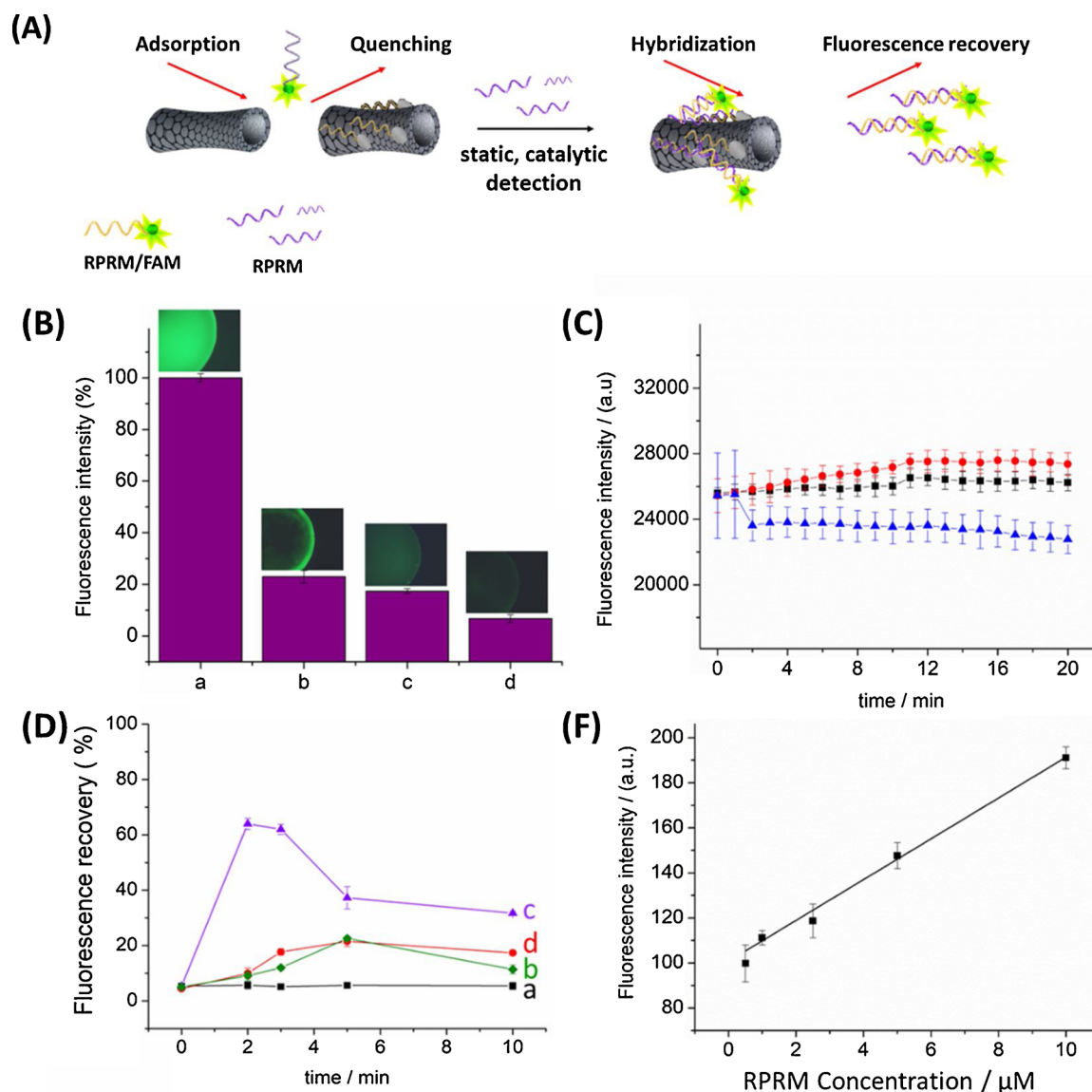
Fig. 5. (A) Schematic illustration for the detection strategy. (B) Fluorescence intensity changes expressed as percentage for the incubation of RPRM/FAM with erGO/Pt micromotors at (a) 0; (b) 2.0; (c) 15 min and (d) overnight incubation. (C) Fluorescence intensity versus time for RPRM/FAM probe (black square), RPRM/FAM + TE buffer solution (red circle) and RPRM/FAM + H$_2$O$_2$ solution (blue triangle). (D) Fluorescence recovery intensities expressed as a percentage for RPRM/FAM/erGO/Pt micromotors toward the addition of (a) TE buffer solution; (b) RPRM in static condition; (c) RPRM in catalytic condition and (d) NC in catalytic condition. (F) Calibration plot for the RPRM detection in catalytic conditions. (For interpretation of the references to colour in the Figure, the reader is referred to the web version of this article).

due to π-π stacking and electrostatic interactions, which leads to a quenched fluorescence [46,47].

]. Upon the addition of target RPRM, the hybridization process takes place, releasing the double-stranded from the microtube to allow the recovery of the fluorescence intensity from the FAM dye, and in consequence the biomarker detection [35].

Fig. 5B shows the changes in the fluorescence intensity expressed in percentage for the RPRM/FAM probe solution during the incubation time with erGO/Pt microtubes. The RPRM/FAM probe (Fig. 5Ba), display strong green fluorescence intensity, which after 2.0 min of incubation with erGO/Pt micromotors (Fig. 5Bb) notoriously decreased to 23.0 ± 2.3 %. The quenching effect is originated from fluorescence (or Förster) resonance energy transfer (FRET), or non-radiative dipole-dipole coupling, between the FAM dye, coupled to RPRM probe and the erGO outer layer of the micromotor, according to what has been described in the literature [46, 47]. After 15 min of incubation, the fluorescence intensity continues decreasing to 17.4 ± 1.0 % (Figure

5Bc), and for the final incubation, overnight condition, a quenching of 94.6 ± 1.6 % is reached from that obtained at the initial time (Figure 5Bd). The quenching effect remained constant for a period of one week. The standard deviation was calculated from four different batches of prepared RPRM/FAM/erGO/Pt micromotors.

In Fig. 5C, we investigated the stability of the RPRM/FAM probe in the absence of micromotors, monitoring the fluorescence intensity as a function of time. It can be observed that for RPRM/FAM probe (black square), the fluorescence intensity does not suffer alterations, remaining constant. However, after the addition at 1 min of TE buffer solution (red circle), the fluorescence intensity starts to increase smoothly. On the contrary, when H$_2$O$_2$ (1.5 % wt, at 1 min) was added, the fluorescence intensity decreased by 7.8 ± 0.9 % in the first minute and then remained constant (blue triangle). These results were considered for the posterior detection of Rep C in static or catalytic detection. Fig. 5D shows the fluorescence recovery expressed in percentages as a function of time from the analysis RPRMFAM/erGO/Pt

micromotors in different experimental conditions (standard deviation was calculated from n = 4 measurements). Supplementary Figure S3 shows representative fluorescence images of this study, and a total of 100 % fluorescence intensity corresponds to the obtained for the incubation of RPRM/FAM and RPRM at 5μM both. Fig. 5Da (black curve) showed no significant variation of fluorescence recovery after the addition of TE buffer solution performed as a control in catalytic condition (static condition showed similar results). Besides, this result indicates that the RPRM/FAM probe is not released from the microtube because of the movement. Fig. 5Db (green curve) showed that for the detection of RPRM (5.0 μM) in static conditions, only 22.0 ± 1.9 % of fluorescence recovery is reached, and was observed at 5 min of reaction. Instead, for the detection of RPRM (5 μM) in catalytic conditions (Fig. 5Dc, purple curve) a fluorescence maximum of 64.0 ± 2.0 % is recovered at 2 min of reaction, faster and sixfold higher than static detection demonstrating that the self-propulsion of the micromotor increases the effective encounter between the strands allowing the hybridization process in shorter time. However, a decrease in the fluorescence intensity is observed in later detection times, which is possibly due to new interaction with the microtube and consequently to quenching.

To study the specificity of the assay, a non-complementary ssDNA strand (NC, 5.0 μM) was added in catalytic conditions. Figure 5Dd (red curve) showed a similar response to that obtained for the detection of RPRM in the static condition. This response could indicate that the hybridization process occurs but with a maximum fluorescence recovery in posterior time compared to the catalytic detection and sixfold lower. Thus, the catalytic detection could be used as a selective and qualitative platform for target GC biomarker detection, without the interference of another ssDNA.

Fig. 5F shows the calibration plot obtained in catalytic conditions at 2.0 min of detection for different concentrations of target RPRM. A linear relationship is observed over the range from 1.0 to 10 μM (r^2 = 0.993) with a detection limit (LOD) of 1.3 μM (taken as 3.3 σ/S, where σ is the standard deviation of the blank signal and S is the sensitivity), a quantification limit (LOQ) of 3.8 μM (taken as 10 σ/S) and relative standard deviation (RSD) of 4.2 %. Lower concentrations of the target biomarker can be detected by increasing the detection time. Supplementary Figure S5 displays a series of representative droplet images of this study showing that the fluorescence intensity obtained for the catalytic detection at 2.0 min in (a) buffer TE solution, (b) target RPRM and (c) noncomplementary DNA sequence were similar (89 ± 12; 95 ± 15; 83 ± 11 a.u, respectively). However, when the detection was performed at 5.0 min a clear difference was observed between the fluorescence intensity response from both 100 and 500 nM) concentrations of RPRM target studied (143 ± 11 a.u. at 2.0 min and 155 ± 16 a.u. at 5.0 min) and the controls (85 ± 9.0 and 91 ± 12 a.u. for TE buffer solution and NC, respectively).

In summary, the findings in this work suggest that geometrical features should be considered in the development of single or hybrid micromotors and when these are desired to be applied as an alternative sensing system to real samples.

4. Conclusion

Catalytic (erGO/Pt), magnetic (erGO/Ni), and hybrid (erGO/Ni-Pt; erGO/Pt-Ni) micromotors with single or dual motion were prepared through an electrochemical template assistance method. The scanning electron microscopy characterization revealed that erGO/Pt microtubes have a continuous growth dependency with plating time and potential energy. Instead, erGO/Ni showed microtubular morphology but with a dramatic change in the wall thickness when the electrical charge was varied. For the hybrid microtubular motors, similar physical features were observed. However, they were thicker and shorter than their individual versions. The comparison of catalytic motion demonstrated, first, that the main pattern of motion was circular and that erGO/Pt

microtubular motors were faster than the hybrid forms. This behavior is due to the exposure of the platinum layer to the H_2O_2 solution inside the microtube, as opposed to erGO/Pt-Ni hybrid micromotors. On the other hand, when dual motion is activated by an approaching magnet, while the micromotors are self-propelled, the magnetic field forces the micromotor movement into a straight pattern. Additionally, an increasing travel distance is obtained as a result of the high speed observed; this effect was more relevant for erGO/Ni-Pt than for erGO/Pt-Ni. These results were taken into account to select a micromotor for the RPRM biomarker detection. The catalytic detection response was sixfold higher than the detection in static conditions, showing high selectivity as well as a fast detection response, making it a promising alternative for qualitative or quantitative detection of other circulant cancer biomarkers, based on DNA hybridization.

Declaration of Competing Interest

The authors declare that they have no known competing financial interests or personal relationships that could have appeared to influence the work reported in this paper.

Appendix A. Supplementary data

Supplementary material related to this article can be found, in the online version, at doi:https://doi.org/10.1016/j.snb.2020.127843.

References

[1] W. Gao, S. Sattayasamitsathit, J. Orozco, J. Wang, Highly efficient catalytic microengines: template electrosynthesis of polyaniline/platinum microtubes, J. Am. Chem. Soc. 133 (2011) 11862–11864, https://doi.org/10.1021/ja203773g.

[2] D. Kagan, S. Campuzano, S. Balasubramanian, F. Kuralay, G.U. Flechsig, J. Wang, Functionalized micromachines for selective and rapid isolation of nucleic acid targets from complex samples, Nano Lett. 11 (2011) 2083–2087, https://doi.org/10.1021/nl2005687.

[3] H. Ye, J. Kang, G. Ma, H. Sun, S. Wang, Journal of Colloid and Interface Science High-speed graphene @ Ag-MnO 2 micromotors at low peroxide levels, J. Colloid Interface Sci. 528 (2018) 271–280, https://doi.org/10.1016/j.jcis.2018.05.088.

[4] T. Xu, L. Xu, L. Zhang, Ultrasound propulsion of micro- / nanomotors, Appl. Mater. Today. 9 (2017) 493–503, https://doi.org/10.1016/j.apmt.2017.07.011.

[5] M. Pumera, A.M. Pourrahimi, K. Villa, Y. Ying, ZnO / ZnO 2 / Pt Janus Micromotors Propulsion Mode Changes With Size and Interface Structure : Enhanced Nitroaromatic Explosives Degradation Under Visible Light, (2018), https://doi.org/10.1021/acsami.8b16217.

[6] C. Liang, C. Zhan, F. Zeng, D. Xu, Y. Wang, W. Zhao, J. Zhang, J. Guo, H. Feng, X. Ma, Bilayer tubular micromotors for simultaneous environmental monitoring and remediation, ACS Appl. Mater. Interfaces 10 (2018) 35099–35107, https://doi.org/10.1021/acsami.8b10921.

[7] D. Vilela, J. Parmar, Y. Zeng, Y. Zhao, S. Sanchez, Graphene based microbots for toxic heavy metal removal and recovery from water, Nano Lett. 16 (2016) 2860–2866, https://doi.org/10.1021/acs.nanolett.6b00768.

[8] B.E. De Ávila, P. Angsantikul, J. Li, M.A. Lopez-ramirez, D.E. Ramírez-herrera, S. Thamphiwatana, C. Chen, J. Delezuk, R. Samakapiruk, V. Ramez, M. Obonyo, L. Zhang, J. Wang, Micromotor-enabled active drug delivery for in vivo treatment of stomach infection, Nat. Commun. 2017 (n.d.) 1–8. doi:10.1038/s41467-017-00309-w.

[9] W. Gao, R. Dong, S. Thamphiwatana, J. Li, W. Gao, L. Zhang, J. Wang, Artificial micromotors in the mouse's stomach: a step toward in vivo use of synthetic motors, ACS Nano 9 (2015) 117–123, https://doi.org/10.1021/nn507097k.

[10] V. Magdanz, L. Schwarz, F. Hebenstreit, Sperm-hybrid micromotor for targeted drug delivery, ACS Nano 12 (2018) 327–337, https://doi.org/10.1021/acsnano.7b06398.

[11] B. Esteban-Fernández de Ávila, M.A. Lopez-Ramirez, D.F. Báez, A. Jodra,

V.V. Singh, K. Kaufmann, J. Wang, Aptamer-modified graphene-based catalytic micromotors: off–on fluorescent detection of ricin, ACS Sens. 1 (2016) 217–221, https://doi.org/10.1021/acssensors.5b00300.

[12] D. Vilela, M.M. Stanton, J. Parmar, S. Sa, Microbots decorated with silver nanoparticles kill Bacteria in aqueous media, ACS Appl. Mater. Interfaces 9 (2017) 22093–22100, https://doi.org/10.1021/acsami.7b03006.

[13] B. Esteban-Fernández De Ávila, D.E. Ramírez-Herrera, S. Campuzano, P. Angsantikul, L. Zhang, J. Wang, Nanomotor-enabled pH-Responsive intracellular delivery of Caspase-3: toward rapid cell apoptosis, ACS Nano 11 (2017) 5367–5374, https://doi.org/10.1021/acsnano.7b01926.

[14] X. Yu, Y. Li, J. Wu, H. Ju, Motor-based autonomous microsensor for motion and counting immunoassay of cancer biomarker, Anal. Chem. 86 (2014) 4501–4507, https://doi.org/10.1021/ac500912c.

[15] L. Wu, X. Qu, Cancer biomarker detection: recent achievements and challenges, Chem. Soc. Rev. 44 (2015) 2963–2997, https://doi.org/10.1039/c4cs00370e.

[16] H. Lee, J.-E. Park, J.-M. Nam, Bio-barcode gel assay for microRNA, Nat. Commun. 5 (2014) 3367, https://doi.org/10.1038/ncomms4367.

[17] S. Erbas-Cakmak, D.A. Leigh, C.T. McTernan, A.L. Nussbaumer, Artificial molecular machines, Chem. Rev. 115 (2015) 10081–10206, https://doi.org/10.1021/acs.chemrev.5b00146.

[18] W. Law, K. Yong, A. Baev, P.N. Prasad, L.A.W.E.T. Al, Sensitivity Improved Surface Plasmon Resonance Biosensor for Cancer Biomarker Detection Based on Plasmonic Enhancement, ACS Nano (2011) 4858–4864.

[19] W. Gao, X. Feng, A. Pei, C.R. Kane, R. Tam, C. Hennessy, J. Wang, Bioinspired helical microswimmers based on vascular plants, Nano Lett. 14 (2014) 305–310, https://doi.org/10.1021/nl404044d.

[20] X. Yan, Q. Zhou, J. Yu, T. Xu, Y. Deng, T. Tang, Q. Feng, L. Bian, Y. Zhang, A. Ferreira, L. Zhang, Magnetite nanostructured porous hollow helical microswimmers for targeted delivery, Adv. Funct. Mater. 25 (2015) 5333–5342, https://doi.org/10.1002/adfm.201502248.

[21] J. Parmar, D. Vilela, S. Sanchez, Tubular microjets: fabrication, factors affecting the motion and mechanism of propulsion, Eur. Phys. J. 225 (2016) 2255–2267, https://doi.org/10.1140/epjst/e2016-60064-x.

[22] K. Yao, M. Manjare, C.A. Barrett, B. Yang, T.T. Salguero, Y. Zhao, Nanostructured scrolls from graphene oxide for microjet engines, J. Phys, Chem. Lett. 3 (2012) 2204–2208, https://doi.org/10.1021/jz300749p.

[23] D. Walker, M. Kübler, K.I. Morozov, P. Fischer, aM Leshansky, Optimal length of low reynolds number nanopropellers, Nano Lett. 15 (2015) 4412–4416, https://doi.org/10.1021/acs.nanolett.5b01925.

[24] V.M. Fomin, M. Hippler, V. Magdanz, S. Sanchez, O.G. Schmidt, Propulsion mechanism of catalytic microjet engines, IEEE Trans. Robot. 30 (2014) 40–48, https://doi.org/10.1109/TRO.2013.2283929.

[25] M. Manjare, B. Yang, Y. Zhao, Bubble-propelled microjets: model and experiment, J. Phys. Chem. C. 117 (2013) 4657–4665, https://doi.org/10.1021/jp311977d.

[26] B.E. De Ávila, P. Angsantikul, J. Li, W. Gao, L. Zhang, J. Wang, Micromotors go in vivo: from test tubes to live animals, Adv. Funct. Mater. 1705640 (2018) 1–12, https://doi.org/10.1002/adfm.201705640.

[27] A. Martín, B. Jurado-Sánchez, A. Escarpa, J. Wang, Template electrosynthesis of high-performance graphene microengines, Small 11 (2015) 3568–3574, https://doi.org/10.1002/smll.201500008.

[28] J. Wang, Nanomachines, Fundamentals and Applications, Wiley-VCH, Weinheim, Germany, 2013, pp. 1–155.

[29] V.V. Singh, A. Martin, K. Kaufmann, S.D.S. de oliveira, J. Wang, Zirconia/Graphene oxide hybrid micromotors for selective capture of nerve Agents.pDf, Chem. Mater. 27 (2015) 8162–8169, https://doi.org/10.1021/acs.chemmater.5b03960.

[30] A. Molinero-fernández, A. Jodra, M. Moreno-, M. López, A. Escarpa, Accepted article, Chem. - A Eur. J. 24 (2018) 7172–7176, https://doi.org/10.1002/chem.201706095.

[31] K. Saavedra, J. Valbuena, W. Olivares, M.J. Marchant, A. Rodríguez, V. Torres-Estay, G. Carrasco-Avino, L. Guzmán, F. Aguayo, J.C. Roa, A.H. Corvalán, Loss of expression of reprimo, a p53-induced Cell Cycle Arrest Gene, correlates with Invasive Stage of Tumor Progression and p73 expression in gastric cancer, PLoS One 10 (2015) 1–13, https://doi.org/10.1371/journal.pone.0125834.

[32] J.D. Amigo, J.C. Opazo, R. Jorquera, I.A. Wichmann, B.A. Garcia-Bloj, M.A. Alarcon, G.I. Owen, A.H. Corvalán, The reprimo gene family: a novel gene lineage in gastric cancer with tumor suppressive properties, Int. J. Mol. Sci. 19 (2018) 1–15, https://doi.org/10.3390/ijms19071862.

[33] Y. Qu, S. Dang, P. Hou, Gene methylation in gastric cancer, Clin. Chim. Acta 424 (2013) 53–65, https://doi.org/10.1016/j.cca.2013.05.002.

[34] C. Bernal, F. Aguayo, C. Villarroel, M. Vargas, I. Díaz, F.J. Ossandon, E. Santibáñez, M. Palma, E. Aravena, C. Barrientos, A.H. Corvalan, Reprimo as a potential biomarker for early detection in gastric cancer, Clin. Cancer Res. 14 (2008) 6264–6269, https://doi.org/10.1158/1078-0432.CCR-07-4522.

[35] C.H. Lu, H.H. Yang, C.L. Zhu, X. Chen, G.N. Chen, A graphene platform for sensing biomolecules, Angew. Chemie - Int. Ed. 48 (2009) 4785–4787, https://doi.org/10.1002/anie.200901479.

[36] D.F. Báez, H. Pardo, I. Laborda, J. Marco, C. Yáñez, S. Bollo, Reduced graphene oxides: influence of the reduction method on the electrocatalytic effect towards nucleic acid oxidation, Nanomaterials 7 (2017) 168, https://doi.org/10.3390/nano7070168.

[37] W. Gao, S. Sattayasamitsathit, A. Uygun, A. Pei, A. Ponedal, J. Wang, Polymer-based tubular microbots: role of composition and preparation, Nanoscale 4 (2012) 2447–2453, https://doi.org/10.1039/c2nr30138e.

[38] H. Zhou, J.H. Park, F.F. Fan, A.J. Bard, Observation of single metal nanoparticle collisions by open circuit, J. Am. Chem. Soc. 134 (2012) 13212–13215, https://doi.org/10.1021/ja305573g.

[39] R. Dasari, K. Tai, D.A. Robinson, K.J. Stevenson, Electrochemical monitoring of single nanoparticle collisions at mercury- Modi fi ed platinum ultramicroelectrodes, ACS Nano 8 (2014) 4539–4546, https://doi.org/10.1021/nn500045m.

[40] H. Wang, J. Guo, S. Moo, M. Pumera, From nanomotors to micromotors: the influence of the size of an autonomous bubble-propelled device upon its motion, ACS Nano 10 (2016) 5041–5050, https://doi.org/10.1021/acsnano.5b07771.

[41] Y. Wang, C.C. Mayorga-martinez, J. Guo, S. Moo, M. Pumera, Structure − function dependence on template-based micromotors, Acs Appl. Energy Mater. 1 (2018) 3443–3448, https://doi.org/10.1021/acsaem.8b00605.

[42] G. Gallino, F. Gallaire, E. Lauga, S. Michelin, Physics of bubble-propelled microrockets, Adv. Funct. Mater. 28 (2018) 1–10, https://doi.org/10.1002/adfm.201800686.

[43] K. Dehority, N. Budin, S.S. Hilston, K. Zhang, A. Fillinger, Deposition of nickel on electrodeposited Cu 2 O films at potentials more positive than the nernst potential of Ni 2 + / Ni 0, J. Electrochem. Soc. (164) (2017) 615–620, https://doi.org/10.1149/2.0751709jes.

[44] A. Irshad, N. Munichandraiah, RSC Advances Electrochemical deposition of manganese oxide – phosphate – reduced graphene oxide composite and electrocatalysis of the oxygen evolution, RSC Adv. 6 (2016) 30552–30563, https://doi.org/10.1039/C6RA01217E.

[45] Z. Wang, Q. Chi, L. Liu, Q. Liu, T. Bai, Q. Wang, A viscosity-based model for bubble-propelled catalytic micromotors, Micromachines 8 (2017) 1–13, https://doi.org/10.3390/mi8070198.

[46] K.P. Loh, Q. Bao, G. Eda, M. Chhowalla, Graphene oxide as a chemically tunable platform for optical applications, Nat. Chem. 2 (2010) 1015–1024, https://doi.org/10.1038/nchem.907.

[47] F. Li, H. Pei, L. Wang, J. Lu, J. Gao, B. Jiang, X. Zhao, C. Fan, Nanomaterial-based fluorescent DNA analysis: a comparative study of the quenching effects of graphene oxide, carbon nanotubes, and gold nanoparticles, Adv. Funct. Mater. 23 (2013) 4140–4148, https://doi.org/10.1002/adfm.201203816.

Dr. Daniela F. Báez received her BSc Degree in Chemistry from Univesity of Santiago of Chile in 2010 and a Doctoral degree in Chemistry from the University of Chile in 2016. During the doctoral's program, she obtained a fellowship for an internship at the Univesity of California, San Diego (UCSD) focused on the research in the development of micro/nanomotors. In 2017, she earned a Chilean Postdoctoral grant for three years to establish a starting research line investigating micromotors as sensing systems. Currently, she is a Postdoctoral Researcher in the Department of Pharmacological and Toxicological Chemistry at the Univesity of Chile, and the Advanced Center for Chronic Diseases. Her research is focused on the fabrication of catalytic and magnetic micromotors as sensing system for cancer biomarkers detection.

Prof. Dr. Marcelo J. Kogan was born in Buenos Aires, Argentina in 1964. He is Professor at the Department of Pharmacology and Toxicology of the School of Pharmacy at the University of Chile and Principal Investigator at the Advanced Center for Chronic diseases (ACCDiS). He is the Coordinator of the Pharmaceutical Sciences Program at the University of Chile. He is the Director of the Laboratory of NANOMEDICINE AND NANOTHERANOSTICS at this center. He is Biochemist and Pharmacist at the University of Buenos Aires and PhD in Organic Chemistry from the same University. He did his postdoctoral research at the Institut of Biomedical Research Barcelona in the field of peptides. His interest is centered on applications of nanobiomaterials and peptides in biomedicine for diagnosis and treatment of conformational diseases including drug delivery, Alzheimer, Cancer, and cardiovascular diseases. He is a pioneer in the field of use nanoparticles for disaggregation of amyloids.